The first high-resolution stalagmite record from Taiwan: Climate and environmental changes during the past 1300 years

Hong-Chun Li [a,*], Min Zhao [a,b], Chia-Hsin Tsai [a], Horng-Sheng Mii [c], Queenie Chang [a], Kuo-Yen Wei [a]

[a] Department of Geosciences, National Taiwan University, Taipei 10617, Taiwan, ROC
[b] State Key Laboratory of Environmental Geochemistry, Institute of Geochemistry, Chinese Academy of Sciences, 46 Guanshui Road, Guiyang 550002, China
[c] Department of Earth Sciences, National Taiwan Normal University, Taipei 11677, Taiwan, ROC

ABSTRACT

This paper presents the first high-resolution Holocene stalagmite record of Taiwan from Jianfei Cave (22°50.873 N; 120°21.255 E) in Dagangshan Mountain, South Taiwan. The 13.6-cm long stalagmite (DGS-1) has been dated by AMS ^{14}C dating, spanning from AD 700 to AD 1933. The δ^{18}O, δ^{13}C and XRF scanned elemental profiles reveal interannual variations in climate and environmental conditions, with light δ^{18}O and δ^{13}C excursions reflecting wet climate and better vegetation coverage under stronger East Asia Summer Monsoon (EASM). Dark layers in DGS-1 containing high Fe, Mn and Sr contents were formed during dry episodes. Five periods with different climate regimes and vegetation conditions can be identified in the DGS-1 record: Period I (AD 700–1200) and Period V (AD 1810–1933) had warm and wet climates with good vegetation coverage. A drying trend probably corresponding to the switch from El Niño-like to La Niña-like oceanic condition occurred during Period II (AD 1200–1400). Cold but relatively wet climates with good vegetation coverage were prevailed during Period III (AD 1400–1610), whereas cold and dry climates with poor vegetation coverage were dominated during Period IV (AD 1610–1810). Based on the rainfall record of Tainan since AD 1897 and the stalagmite record, we found that stronger total solar irradiation (TSI) resulting in strong EASM produces heavy rainfall in South Taiwan on interannual-to-decadal scales; and vice versa. The 117-yr instrumental rainfall record of Tainan showed that rainfall in Tainan decreased during April-to-June and strongly increased during July-to-September in many La Niña years (positive SOI and negative Niño 3.4). This may be because weaker Meiyu rainfall but stronger tropical Equatorial Pacific cyclones (or typhoon) under La Niña condition. Thus, it is better to use seasonal rainfall for detecting relationship between Tainan rainfall and ENSO. On decadal-to-centennial scales, strong El Niño-like state and warm Pacific Decadal Oscillation (PDO) phase are in favor of wet conditions in South Taiwan.

© 2015 Elsevier Ltd. All rights reserved.

1. Introduction

Located in the tropical monsoonal region, Taiwan is often stroked by typhoons and tropical cyclones which can cause huge impacts on human life through flood and landslide disasters (e.g., Tsou et al., 2011). Thus, understanding the climatic patterns and their forcing factors in Taiwan is very important for future climate predictability and management of natural resources. Due to strongly tectonic activities, humid and hot climates, high erosion sedimentation rates in Taiwan eliminate long climatic archives (Tsukada, 1966), and most territorial climatic records are generally

retrieved from small and shallow freshwater lakes in mountain ranges (Chen et al., 2009, 2012; Chen and Wu, 1999; Li et al., 2013; Liew et al., 2006a,b; Lo et al., 1996; Wang et al., 2013, 2014a,b; Yang et al., 2011, 2013, 2014). Those records were mainly based on pollen, diatom, peat, sedimentary feature, and organic chemistry, with resolutions generally longer than decadal scales. Previous studies have shown that rainfall variations in NE Taiwan are influenced by El Niño–Southern Oscillation (ENSO) events (Wang et al., 2014b) and migration of the intertropical convergence zone (ITCZ) (Yang et al., 2014). Although climate in Taiwan is under the influence of East Asian Summer Monsoon (EASM), the rainfall pattern and seasonality are different between North and South Taiwan, e.g., wet winter in north but dry winter in south. Based on the instrumental rainfall records in Taipei and Tainan since 1897, the average spring rainfall (March to

May)/summer rainfall (June to August) ratios are 0.75 ± 0.45 and 0.27 ± 0.18 in Taipei and Tainan, respectively. The averaged winter rainfall (December to February)/summer rainfall ratios for Taipei and Tainan are 0.42 ± 0.30 and 0.06 ± 0.05, respectively. Also, how changes in ENSO and ITCZ affect rainfall in South Taiwan are not clear. Hence, high-resolution paleoclimatic records combing with instrumental and historic records will help us in understanding forcing factors of climate change on decadal or longer scales. In South Taiwan, two lacustrine records have been studied: The Great Ghost Lake (Dagui Lake) by Lo et al. (1996) and Tung-Yuan Pond (Kuiqi Lake) by Yang et al. (2011). Lo et al. (1996) published the sediment record from the Great Ghost Lake over the past 2500 years. They used brightness and TOC/TN of layered sediments to interpret climatic changes: dark layers (high organic C contents) indicating deeper lake under warm/wet climates; and light layers reflecting dry periods when the populations of China were decline. Wann (2000) continued the Great Ghost Lake study by adding analysis of elemental contents in the sediments and pushing the record back to 4600 year ago. He concluded that 550–50, 1500–1000 and 3200–2300 yr BP were three major dry periods in southern Taiwan due to weak summer monsoon corresponding to low sunspot numbers. Based on the Great Ghost Lake record, Wann (2000) found that the long-term trend of dry/wet condition of southern Taiwan was similar to that in monsoonal China with the monsoon rainbelt shifting. However, he pointed out that the dry/wet condition between southern Taiwan and monsoonal China during the Little Ice Age was opposite (i.e. dry in one regime corresponds to wet in the other), perhaps due to strongly increased Meiyu rainfall and decreased typhoon rainfall caused by weakening of summer monsoon with southward shift of the monsoon rainbelt and Subtropical High. Wann (2000) performed spectral analysis on TOC recorded in Great Ghost Lake and obtained cycles of 363, 184, 148, 85, 69, 64, 58 and 51 years which were similar to the cycles of solar activities. The Great Ghost Lake record provided multi-decadal-to-centennial climate variations over the past 4600 years with preliminary discussions on climatic forcing factors. On the other hand, Yang et al. (2011) used $\delta^{13}C$ of organic carbon, TOC% (total organic carbon), and TOC/TN in a sediment core from Tung-Yuan Pond to decipher paleoprecipitation change between 21 kyrs and 2 kyrs. These two lacustrine records are the only available Holocene paleoclimatic records in South Taiwan. None of the above records provided annual-to-decadal climatic variability and were able to compare with instrumental records. The findings from the Great Ghost Lake record are waiting for further evaluation and development. Therefore, a continuous, high-resolution paleoclimate records in South Taiwan especially for the past 2000 years is needed.

This study presents a continuous, high-resolution (1.5-yr) paleoclimate record spanning the past 1300 years based on a 13.6-cm long stalagmite from Jianfei Cave in Dagangshan Mountain, South Taiwan. This is the first high-resolution Holocene speleothem record in Taiwan. The stalagmite has been dated by AMS ^{14}C and MC-ICP-MS ^{230}Th/U methods. A total of 844 samples were analyzed for $\delta^{18}O$ and $\delta^{13}C$. Measurements of elemental contents have been conducted by using ICP-OES and iTRAX XRF core scanner. Based on the detailed isotope and geochemical records as well as the 117-year long rainfall and temperature records of Tainan, climatic patterns and forcing factors of precipitation in south Taiwan will be discussed.

2. Background of the study area

Dagangshan Mountain (Mt.) belongs to Gangshan district of Kaohsiung City in south Taiwan, but is located only ~20 km southeast of Tainan City (Fig. 1A). Climatically speaking, the weather in Dagangshan Mt. is more close to that of Tainan City. The mountain is 4.4 km long in S–N direction and about 2 km wide in E–W direction with a maximum elevation of 312 m above sea level (Fig. 1B). This small mountain hill was formed by uplift of coral reef on an anticline during the late Pleistocene (Fig. 1C). Geological stratum of the study area consists of Chiting Formation which is alternated sandstone and mudstone intercalated with limestone deposited in mid- to late Pleistocene, Dagangshan Limestone that is coral reef limestone formed in shallow marine environment during late Pleistocene, and Holocene alluvium and terrace deposits containing sand, gravel and mud (Fig. 1B). The 40-m thick Dagangshan Limestone has very porous structure covered by ~30 cm soil in some areas. Although several caves had been found in Dagangshan Mt. in AD 1960–1970s, these caves were less than 500 m long and had a few stalagmites, probably due to fast uplift rate of the mountain, very porous and thin limestone bedrock and strong erosion of the surface in the area.

Climatically, the study area belongs to tropical monsoonal climate with annual rainfall and temperature of 1742 mm/yr and 23.7 °C, respectively (Fig. 2). In late spring and early summer, moisture is mainly from South China Sea accompanied with the northward warm surface current. During the summer and early fall, the moisture from western Pacific will cross the central mountain range with heavy storms or typhoons. Unlike the monsoonal region in the eastern China, the surrounding ocean environments of Taiwan affect strongly the climatic conditions. For instance, the warm Kuroshio Current from north equator has a winter branch passing through Bashi Channel and reaches southwest coastal area of Taiwan (Hu et al., 2000; Qiu, 2002; Qu et al., 2004). Consequently, south Taiwan is not cold during the winter whereas north Taiwan is ~5 °C colder under winter monsoon influence. During the winter season, north Taiwan is much wetter than south Taiwan due to the southeastward retreat of rainy front. In the study area, warm season rainfall (from May to October) accounts for 87% of the annual rainfall calculated from instrumental rainfall record of Tainan city from AD 1897 to AD 2014. Fig. 3 exhibits the 5-year running average trends of rainfall and air temperature. Some observations can be seen from comparisons in Fig. 3: (1) the annual rainfall mimics the warm season rainfall (M–O rainfall) very well, indicating that changes in M–O rainfall dominate. (2) The M–O rainfall and the cold season rainfall (from November to April) had opposite trends between AD 1910 and AD 1925. (3) The variations of April–June (4–6) rainfall and July–September (7–9) rainfall are quite different, perhaps reflecting different forcing factors on the seasonal rainfall. It is necessary to understand the different forcing factors on these monsoonal rains. (4) Although the seasonal and annual air temperatures show fluctuations on decadal scales, they have increasing trends following the global warming trend. (5) The surface oceanic conditions such as North Pacific Index (defined as the area-weighted sea level pressure over the region of 30°N–65°N, 160°E–140°W) (Trenberth and Hurrell, 1994), Southern Oscillation Index (Allan et al., 1991) and Pacific Decadal Oscillation index (Mantua et al., 1997) seem to show influences on Tainan rainfall and winter temperature on decadal scales. For example, during AD 1945–1970, the N. Pacific index was high, and the PDO was in cold phase (warmer-than-normal in NW. Pacific, but colder-than normal in E. equatorial Pacific) which was corresponding to a La Niña phase. The N–A air temperature was colder and rainfall in Tainan was lower during this period. However, the above observations were not valid on shorter resolutions. For instance, a warm PDO phase and El Niño state around AD 1940 was corresponding to a rainfall increase in Tainan, but a cold PDO phase and La Niña state around AD 1974 also matched a rainfall increase. Therefore, when discussing climatic forcings one should consider the time resolution. In order to understand the effects of oceanic conditions on rainfall in Tainan, we compare the rainfall record with records of Niño 3.4
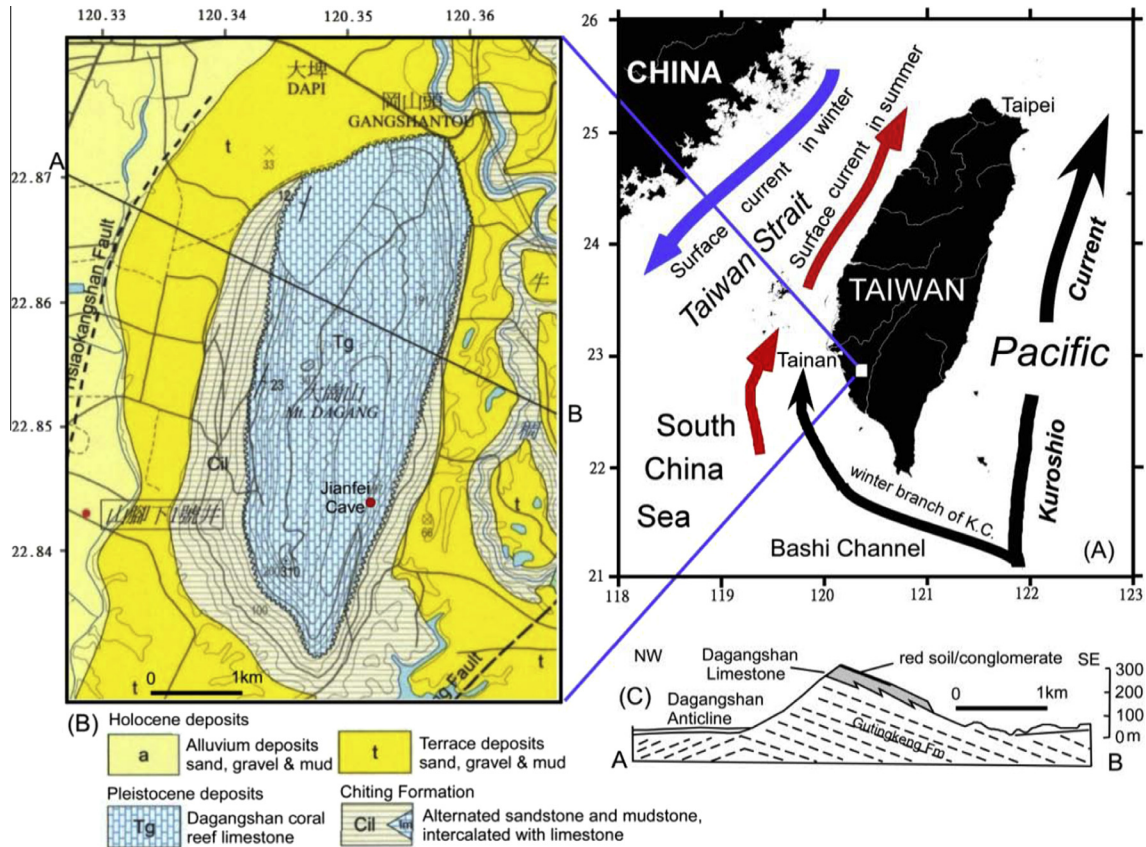
Fig. 1. (A) Map of Taiwan. The cave location is ~20 km southeast of Tainan City. The major oceanic surface currents around Taiwan were briefly marked. (B) Geological map of the study area. The position of Jianfei Cave where Stalagmite DGS-1 was collected is shown. (C) Cross section of A–B transaction (indicated in (B)) in Dagangshan Mountain. (Modified from an on-line map of the Geological Survey of Taiwan.)
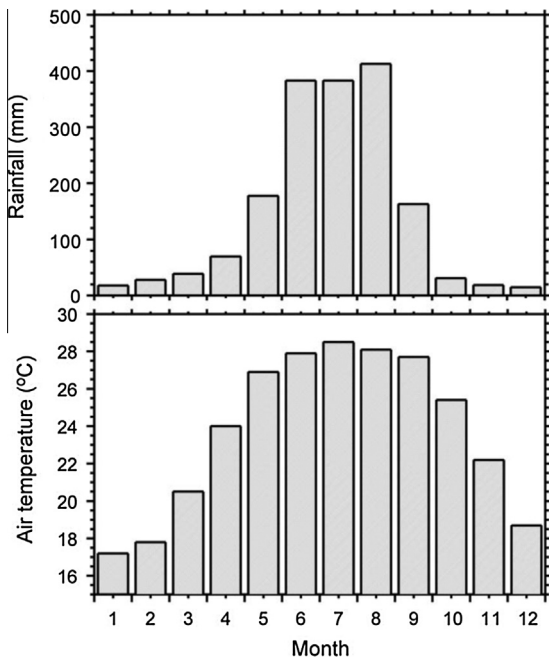

Fig. 2. Monthly rainfall and air temperature in Tainan City, which were averaged from AD 1895–2014. (Data source: http://south.cwb.gov.tw/index.html).

(defined as a three-month average of sea surface temperature departures from normal for region of 120°W–170°W and 5°N–5°S, Trenberth, 1997; Cook et al., 2008), SOI and PDO on

annual scale (Fig. 4). In Fig. 4, positive anomaly of Niño 3.4 (warmer-than-normal in Niño 3.4 region of the equatorial Pacific) and negative anomaly of SOI represent El Niño condition which is generally corresponding to warm phase of PDO (warmer in east equatorial Pacific) on interannual scale. If annual rainfall of Tainan is compared with the oceanic indexes, it is not easy to distinguish the rainfall variation between El Niño and La Niña conditions. For instance, the annual rainfalls were similar under strong El Niño condition during AD 1997–1998 and strong La Niña condition during AD 1999–2000 (Fig. 4). However, if we consider seasonal rainfall, the situation will be different. The annual rainfall of Tainan is mainly controlled by rainfall in June (accounts for 22% of annual rainfall), July (22%) and August (24%) based on the rainfall record of AD 1897–2014. As we mentioned earlier, rainfall during April to June (AMJ) is Meiyu rain and the moisture source is mainly from South China Sea. Rainfall during July to September (JAS) comes from Pacific cyclones and typhoons. For seasonal rainfalls, one can find that in many La Niña years the AMJ rainfalls were low and JAS rainfalls were high shown by the numbers in Fig. 4. In many El Niño years, the AMJ rainfalls were relatively high shown by the star symbols. Since the effects of La Niña condition on the AMJ rainfall (decrease) and JAS rainfall (increase) under were opposite, the correlation of annual rainfall of Tainan with ENSO was obscured in interannual scale. From the comparison in Fig. 4, we can see that El Niño condition is generally in favor of AMJ rainfall increase and La Niña condition leads to decreased AMJ rainfall but increased JAS rainfall on interannual scale in the study area. The influence of ENSO condition on the AMJ rainfall may be through the Luzon Strait transport (LST, i.e., winter branch of KC in Fig. 1) from the Pacific into the South China Sea (SCS) (Qu et al., 2004). North Equatorial Current's (NEC's) bifurcation tends
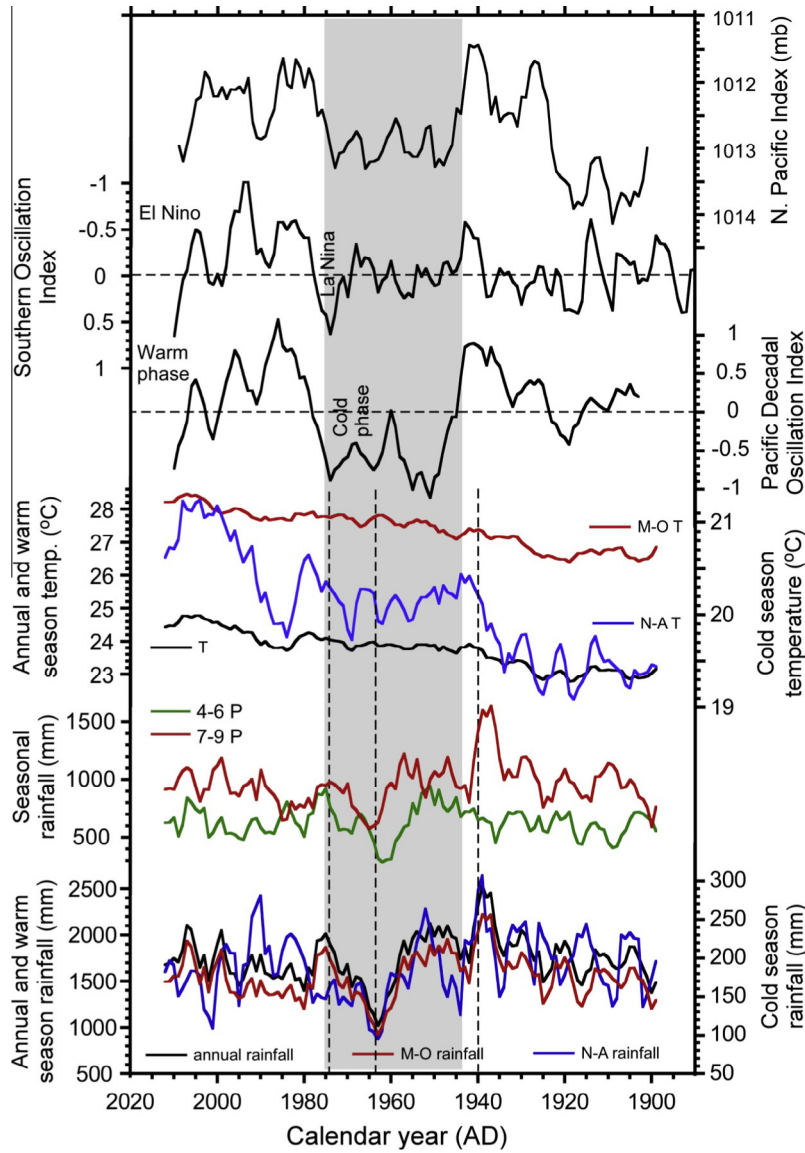
Fig. 3. Comparisons of rainfall and air temperature of Tainan City with proxies of surface ocean conditions. M–O stands for May to October, whereas N–A is from November to April. (Data source: http://climatedataguide.ucar.edu and http://www.cru.uea.ac.uk/cru/data/soi/) (See text for discussion).

to migrate further north during El Niño years and further south during La Niña years (Qiu, 2001). Hence, more storms can be generated by the warm water in the north SCS due to higher LST during El Niño years, resulting in more Meiyu rains. The seasonal circulation in the SCS is mostly driven by monsoonal winds besides the water exchanges through the Taiwan Strait and the Luzon Strait. With stronger winter monsoon and weaker summer monsoon, the monsoonal rainy front may stay longer in South Taiwan in Spring to early Summer. The ENSO influence on the summer rainfall in South Taiwan is through the Pacific cyclones and typhoon rains. Under El Niño condition, the Western Pacific Warm Pool and Walker Circulation shift eastward, so that the cyclonic storms and typhoons generated in the central tropical Pacific are tend to be vanished or turn northward away before reaching Taiwan (Elsner and Liu, 2003; Enfield and Mestas-Nuñez, 1999; Chen et al., 2012; Woodruff et al., 2009). In contrast, cyclonic storms and typhoons generated in the central tropical Pacific under would produce more landfalls in Taiwan during the Summer and Fall. Wang et al. (2000, 2001) found teleconnection between the East Asian monsoon and ENSO: During ENSO

warming, cyclonic anomalies in the northeastern Pacific but the anticyclonic anomalies in the Kuroshio extension were prevailed due to the southeastward shift of the Aleutian low and eastward extension of the East Asian cold high; a weak Western North Pacific Summer Monsoon which is a measure for EASM enhanced rainfall along the mei-yu/baiu front; and the large-scale western North Pacific anomalous anticyclone was linked with weak East Asian winter monsoon.

In summary, the 117-yr Tainan rainfall shows that on interannual variability, weak EASM, El Niño condition, warm PDO phase and increased winter branch of KC enhance the AMJ rainfall; and strong EASM, La Niña condition and cold PDO phase produced higher JAS rainfall but lower AMJ rainfall. How these forcing factors to affect rainfall in South Taiwan needs to be further studied.

3. Sample and analytical method

Stalagmite DGS-1 used for this study was from Jianfei Cave (22°50.873 N; 120°21.255 E) which is located on the southeast
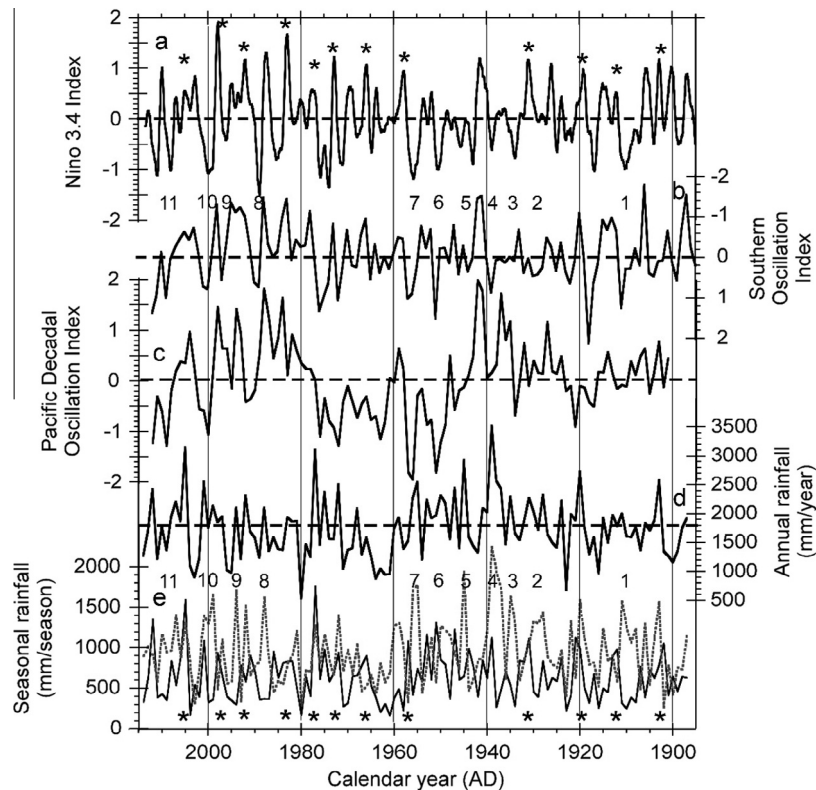
Fig. 4. Comparisons among Nino 3.4 index (a), SOI (b), PDO index (c), Tainan annual rainfall (d) and Tainan seasonal rainfall (e) on annual scale. For the seasonal rainfall, the thin solid curve denotes rainfall during April to June, and the thick dotted curve represents rainfall during July to September. The numbers mark episodes with low AMJ rainfall but high JAS rainfall corresponding to La Niña years. (Data sources are the same as for Fig. 3).
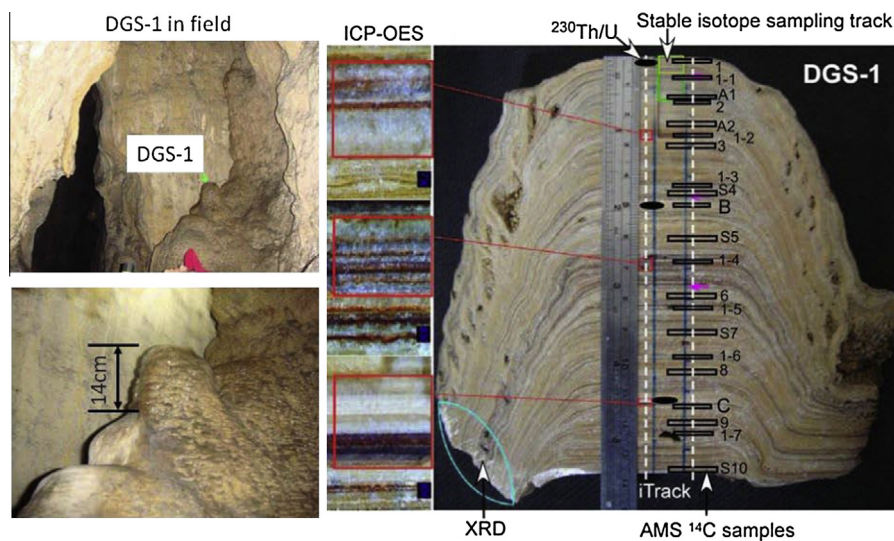
Fig. 5. The left panel shows Stalagmite DGS-1 in the field. The right panel exhibits the cross section of DGS-1 and sampling positions of various analytical methods.

flank of Dagangshan Mt. with an elevation of 169 m (Fig. 1B). The cave is about 50-m long and has very narrow space. The thickness of the cave ceiling is less than 10 m, and in some sites roots from trees above the cave can be seen inside the cave. Although soil layer above the cave is thin, vegetation around the cave is abundant. With strong flowing and dirty seepage water, carbonate deposits are yellowish (Fig. 5). Currently, there is no other active deposition of speleothem inside the cave except calcite precipitation occurs with sheet flow along cave walls. DGS-1 is 136.8 mm in height (Fig. 5). Halving the stalagmite along its growth axis,

colorful growth bands can be clearly seen. However, when zooming up a color band, more detailed laminations appear. Without accurate dating control, we are not certain that these laminations are annual bands.

X-ray diffraction (XRD) analysis on the stalagmite shows the carbonate mineral is calcite. Detailed examination on the stalagmite depositional features did not find growth hiatus and possible recrystallization. Powder samples were drilled from split section of DGS-1 for ^{230}Th/U dating, Accelerate Mass Spectrometer (AMS) ^{14}C dating, and stable isotope analysis (Fig. 5). Three dark layers and

Table 1
^{230}Th/U dating results on Stalagmite DGS-1 by a Finnigan Neptune MC-ICP-MS in the HISPEC Lab at NTU.

Sampl. ID	Depth (mm)	^{238}U ppb[a]	^{232}Th ppt	δ^{234}U meas.[a]	[^{230}Th/^{238}U] activity[c]	[^{230}Th/^{232}Th] ppm[d]	Age Uncorr.	Age Corr.[c,e]	δ^{234}U$_{initial}$ Corr.[b]
DGS-1-01	2 ± 1	1454 ± 2166	80,658 ± 120,196	44 ± 3	0.04414 ± 0.09303	13 ± 28	4716 ± 10,184	3302 ± 9054	44 ± 3
DGS-1-02	51 ± 1	3720 ± 10.3	81,499 ± 1180	41 ± 3	0.01832 ± 0.00072	14 ± 1	1938 ± 77	1380 ± 565	41 ± 3
DGS-1-03	112 ± 1	3926 ± 11.1	266,038 ± 5013	46 ± 3	0.07557 ± 0.00225	18 ± 1	8182 ± 254	6457 ± 1757	47 ± 3

Chemistry was performed on June 19th, 2009 (Shen et al., 2003) and instrumental analyses on MC-ICP-MS (Shen et al., 2012). Analytical errors are 2σ of the mean.

[a] δ^{234}U = ([^{234}U/^{238}U]$_{activity}$ − 1) × 1000.

[b] δ^{234}U$_{initial}$ corrected was calculated based on ^{230}Th age (T), i.e., δ^{234}U$_{initial}$ = δ^{234}U$_{measured}$ × e$^{\lambda 234 \times T}$, and T is corrected age.

[c] [^{230}Th/^{238}U]$_{activity}$ = 1 − e$^{-\lambda 230T}$ + (δ^{234}U$_{measured}$/1000)[λ_{230}/($\lambda_{230} − \lambda_{234}$)](1 − e$^{-(\lambda 230−\lambda 234)T}$), where T is the age. Decay constants are 9.1577 × 10^{-6} yr^{-1} for ^{230}Th, 2.8263 × 10^{-6} yr^{-1} for ^{234}U, and 1.55125 × 10^{-10} yr^{-1} for ^{238}U (Cheng et al., 2000).

[d] Age corrections were calculated using an ^{230}Th/^{232}Th atomic ratio of 4 (±4) ppm. Those are the values for a material at secular equilibrium, with the crustal ^{232}Th/^{238}U value of 3.8. The errors are arbitrarily assumed to be 100%.

[e] δ^{234}U$_{initial}$ corrected was calculated based on ^{230}Th age (T), i.e., δ^{234}U$_{initial}$ = δ^{234}U$_{measured}$ × e$^{\lambda 234 \times T}$, and T is corrected age.

three white layers were drilled for elemental analysis by using a PE Optima7000 DV ICP-OES in the department of Earth Sciences at the National Cheng-Kung University (NCKU) (Fig. 5). Elemental contents are also measured by using an iTRAX X-ray fluorescence (XRF) core scanner made by Cox Analytical Systems (Gothenburg, Sweden) in the Department of Geosciences at the National Taiwan University (NTU).

In this study, three samples for ICP-MS ^{230}Th/U dating (oval dots in Fig. 5) were taken from light color bands in upper, middle and lower parts of DGS-1. The ^{230}Th/U dating was conducted in the High-precision Mass Spectrometry and Environment Change Laboratory (HISPEC) at the NTU in 2009, following the method described in Shen et al. (2002, 2003). Dating results are listed in Table 1.

Twenty-one samples (rectangle boxes in Fig. 5) in three batches were taken from 21 horizons in DGS-1 for AMS ^{14}C dating. The dating method was described in Zhao et al. (2015). In order to understand dead carbon effect on the AMS ^{14}C dating results of the stalagmite, soil, plant, coral reef limestone and newly deposited soda-straw were collected in the study area. All AMS ^{14}C dates are listed in Table 2. The measured ^{14}C ages are converted to calibrated calendar ages (year BP = years before AD 1950) using CalPal Online Radiocarbon Calibration of ^{14}C and CALIB 7.0 (http://calib.qub.ac.uk/calib/) (Stuiver and Reimer, 1986, 1993). Age uncertainties are in 1σ error.

A total of 844 samples were milled along the growth axis of DGS-1, with the sampling resolutions of 0.1 mm between 0.5 and 26 mm and 0.2 mm between 26 and 136.8 mm after the top sample of 0.5 mm (some overlaps between 26 and 30 mm). These samples were analyzed in three stable isotope laboratories: the top 140 samples were run in the Department of Earth Sciences at NCKU by a Finnigan Delta XP plus isotopic ratio mass spectrometer (IRMS) equipped with a Kiel-III Carbonate Device (Lee, 2010); Sample number from 140 to 230 were measured in the Department of Geosciences at NTU which has a Finnigan MAT-253 IRMS equipped with a Kiel-III Carbonate Device; and Sample from 231 to 844 were analyzed in the Department of Earth Sciences at the National Taiwan Normal University (NTNU) contains a Micromass IsoPrime IRMS equipped with a Multicarb automatic system. The calcite powders were dissolved at 70 °C in H$_3$PO$_4$. The δ^{18}O and δ^{13}C values reported here are relative to the Vienna PeeDee Belemnite (VPDB) standard at 25 °C. The standard deviations of NBS-19 runs are normally 0.08‰ for δ^{18}O and 0.06‰ for δ^{13}C. A working standard, MAB (a pure marble formed in Taroko National Park of Eastern Taiwan ca. 250 million years ago with δ^{18}O = −6.9‰ and δ^{13}C = 3.4‰), was measured after every 5–7 sample measurements to monitor any instrumental drift. The δ^{18}O and δ^{13}C results are plotted in Fig. 6.

Elemental contents in the stalagmite were measured by two methods: ICP-OES which is able to measure quantitatively elemental concentrations with errors <2% relative standard deviation (RSD) (Olesik, 1991), and iTRAX XRF core scanner that provides quick, non-destructive, continuous and high-resolution elemental contents (Finné et al., 2014). About 20 mg of sample powder was dissolved by 4 N HNO$_3$. The solution was evaporated to dryness. Adding concentrated HNO$_3$ and HCl dissolve impurities. Again, the solution was evaporated to dryness. Then, the residue was dissolved by 50 mL 2 N HNO$_3$. The solution can be used for measuring Cu, Zn, Ba, Fe, Mn in the ICP-OES, but needs to be diluted for measuring Ca, Mg and Sr. All results are listed in Table 3, except Cu content which was below detection limit of 0.001 ppm.

For the iTRAX XRF scan, a polished thick (~10 mm) slab of the entire DGS-1 was placed in the XRF scanner. The scanning condition was using a Mo tube set at 30 kV and 30 mA, a sampling interval of 200 μm and an exposure time of 40 s. A digital optical RBG image, a digital radiographic image, and a μ-XRF elemental profile

Table 2
AMS ^{14}C dating results of Stalagmite DGS-1, newly formed soda-straw, coral carbonates and organic carbon from soil and plant remain in Dagangshan Mountain.

Lab code	Sample Id	Depth (mm)	pMC (%)	Δ^{14}C (‰)	Age (yr BP)	Calib. age (yr BP)
NTUAMS-353	DGS-1	1	88.33	−116.7	997 ± 21	930 ± 10
NTUAMS-1196	DGS-1-1	6	90.72	−92.8	783 ± 2	705 ± 10
NTUAMS-623	DGS-A1	13	77.96	−220.4	2000 ± 6	1960 ± 20
NTUAMS-354	DGS-2	14	74.97	−250.3	2314 ± 24	2345 ± 10
NTUAMS-624	DGS-A2	23	85.23	−147.7	1284 ± 4	1230 ± 35
NTUAMS-1202	DGS-1-2	26	82.24	−177.6	1571 ± 2	1470 ± 35
NTUAMS-355	DGS-3	29	80.85	−191.5	1708 ± 37	1630 ± 55
NTUAMS-1203	DGS-1-3	43	87.94	−120.6	1032 ± 3	950 ± 10
NTUAMS-619	DGS-S4	45	81.62	−183.8	1631 ± 6	1540 ± 5
NTUAMS-625	DGS-B	49	82.53	−174.7	1542 ± 5	1450 ± 40
NTUAMS-620	DGS-S5	59	80.79	−192.1	1713 ± 6	1640 ± 50
NTUAMS-1204	DGS-1-4	67	82.01	−179.9	1593 ± 5	1480 ± 45
NTUAMS-358	DGS-6	78.5	77.59	−224.1	2038 ± 38	2005 ± 55
NTUAMS-1205	DGS-1-5	82	77.81	−221.9	2015 ± 7	1970 ± 20
NTUAMS-621	DGS-S7	91	81.23	−187.7	1670 ± 5	1560 ± 10
NTUAMS-1206	DGS-1-6	99	80.11	−198.9	1782 ± 6	1715 ± 10
NTUAMS-360	DGS-8	104	82.54	−174.6	1542 ± 10	1450 ± 45
NTUAMS-626	DGS-C	113	81.42	−185.8	1651 ± 5	1550 ± 10
NTUAMS-361	DGS-9	120	79.54	−204.6	1839 ± 10	1780 ± 30
NTUAMS-1207	DGS-1-7	123	71.87	−281.3	2654 ± 33	2780 ± 20
NTUAMS-622	DGS-S10	136	78.99	−210.1	1895 ± 6	1850 ± 15
NTUAMS-1007	20140607-5 new soda-straw		84.54	−154.6	1349 ± 4	1295 ± 5
NTUAMS-1004	20140607-1A coral carbonate		3.64	−963.6	26,611 ± 280	31,315 ± 390
NTUAMS-1005	20140607-1B coral carbonate		7.06	−929.4	21,299 ± 432	25,530 ± 616
NTUAMS-1427	DGM1 Dagangshan soil		91.44	−85.6	719 ± 5	675 ± 5
NTUAMS-1428	DGM2 plant remain		92.02	−79.8	668 ± 4	625 ± 40
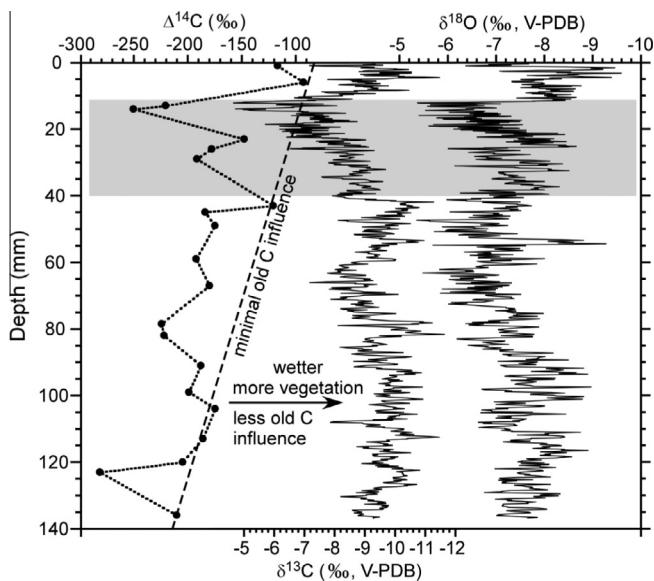
Fig. 6. The δ^{18}O and δ^{13}C records in DGS-1 and their comparison with the Δ^{14}C in DGS-1. When the δ^{13}C becomes heavier, the Δ^{14}C contains more dead carbon.

were generated during the scanning produces. In order to obtain reliable results, two separate scans along two tracks were performed for duplicates (Fig. 5). The scanner is normally set for marine sediment cores which select Al, Si, S, Cl, Ar, K, Ca, Ti, V, Mn, Fe, Ni, Cu, Zn, Rb, Sr, Zr and Ba for measurement. For the stalagmite scan, only Ca, Sr, Fe, Mn, Si, Ti, Zn, Ni and Cu are meaningful. The other listed elements are either too low for detecting or no variations. In addition, the iTRAX XRF scan cannot measure Mg, Na and Li. The mean contents of these elements in DGS-1 are listed in Table 4. The unit for elements by the XRF scan is counts per second (cps). Because the sensitivity of each element is different to the XRF scan, the elemental contents in cps are not absolute concentration, but relative content. The Ca, Sr, Si and Fe XRF scan profiles are shown in Fig. 7, and the Fe and Mn XRF scan profiles are plotted in Fig. 8.

4. Results and discussions

4.1. ^{230}Th/U dating

Three ^{230}Th/U dates in Table 1 appear large uncertainties and reversed age sequence. Although U contents of the samples are high, but the Th contents are very high too. The dirty stalagmite

Table 3
Elemental contents of calcite from six layers in DGS-1 and of cavewater and rainwater measured by using an ICP-OES. The layers are indicated in Fig. 8. The units are mg/kg for stalagmite calcite and mg/L for waters.

Sample ID	Depth (mm)	Layer color	Ca (ppm)	Mg (ppm)	Mg/Ca	Sr (ppm)	Sr/Ca	Mg/Sr	Fe (ppm)	Mn (ppm)	Ba (ppm)	Zn (ppm)
DGS01-D1	25	Dark	453,316	2721	0.0060	6660	0.0147	0.4086	9615	267	41	5
DGS01-D2	27	White	434,866	1866	0.0043	3395	0.0078	0.5497	7659	126	21	4
DGS01-D3	67	White	444,757	2325	0.0052	5743	0.0129	0.4049	11,024	990	56	12
DGS01-D4	68	Dark	422,553	2585	0.0061	6560	0.0155	0.3941	33,213	1314	70	4
DGS01-D5	113	White	443,042	2838	0.0064	6163	0.0139	0.4604	6924	27	42	2
DGS01-D6	114	Dark	419,435	2982	0.0071	9336	0.0223	0.3194	29,323	3557	124	7
Cave water			43.46	9.97	0.2294	5.189	0.1194	1.92	0	0	0.015	0.002
Rain water			2.345	0.316	0.215	0.014	0.008	31.036	0.115	1.088	0.009	0.0143

Table 4
Mean elemental contents (cps) in DGS-1 determined by an XRF core scanner. R^2 is the correlation coefficiency of duplicated runs between the two tracks.

	Ca	Sr	Fe	Mn	Zn	Ni	Si	Ti	Cu
Track 1	37,1085	59,833	16,745	1292	366	120	76	50	33
Track 2	374,839	60,458	16,922	1310	375	120	76	49	34
R^2	0.934	0.994	0.999	0.998	0.951	0.838	0.356	0.534	0.860
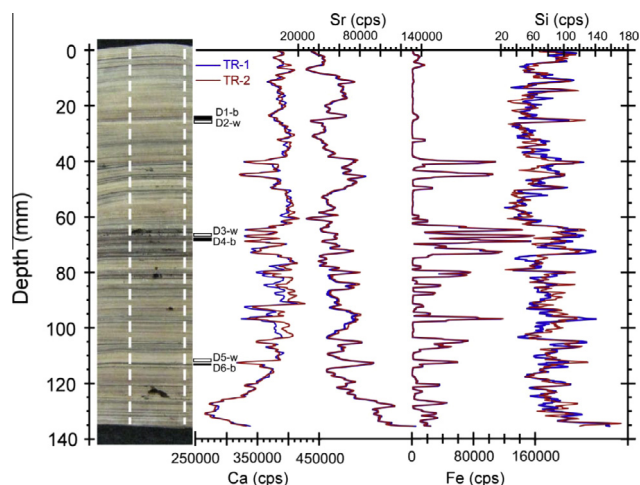
Fig. 7. Profiles of Ca, Sr, Fe and Si contents in DGS-1 determined by using an ITRAX XRF core scanner. The measurements of elements were done for two scan tracks. The six layers with white (e.g., D2-w) or dark (e.g., D1-b) colors were measured for elements by using an ICP-OES.
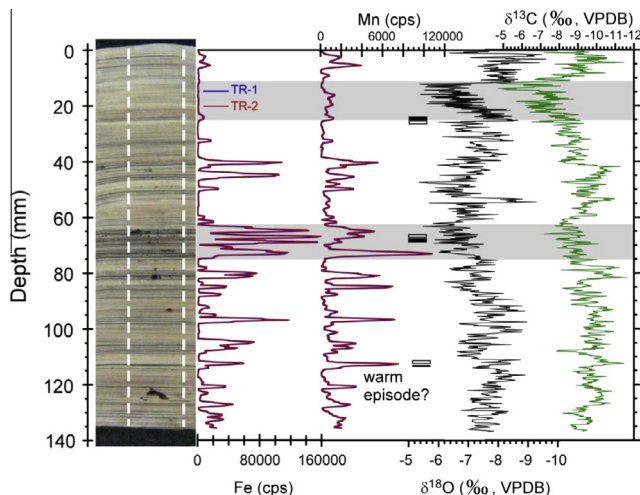
Fig. 8. Profiles of Fe and Mn contents in DGS-1 determined by using an ITRAX XRF core scanner, and their comparisons with the $\delta^{18}O$ and $\delta^{13}C$ records.

has very low $^{230}Th/^{232}Th$ which causes large errors when radiogenic ^{230}Th is small. Among the three dates, the top one (DGS-1-01) is useless. The second one (DGS-1-02) with low ^{232}Th content has relatively small uncertainty, which indicates that the stalagmite at 50–52 mm depth is 1380 ± 565 a old. The third sample has a corrected age of 6457 ± 1757 a, with a ^{232}Th content 3 times higher than the other two. Since the age corrections were used a constant $^{230}Th/^{232}Th$ atomic ratio of 4 ppm, the age could be under-corrected, i.e., the age is too old. Because the top sample (the youngest) has a $^{230}Th/^{232}Th$ ratio of 13 ppm, this ratio should be close to the initial $^{230}Th/^{232}Th$ ratio. If using a higher (>4 ppm) $^{230}Th/^{232}Th$ ratio for initial ^{230}Th correction, the ages could be

younger. Nevertheless, although $^{230}Th/U$ dating on the stalagmite was not good, the $^{230}Th/U$ date of 1380 ± 565 a can be considered as a reference age in the stalagmite.

4.2. AMS ^{14}C dating and chronology of DGS-1

Radiocarbon dating on stalagmites can be influenced by dead carbon effect since dissolution of old carbon from bedrock limestone is a part process during speleothem formation. Dead carbon fraction (DCF) in stalagmites varies with overlying vegetation and soil intensities, open/close system of exchange between atmospheric CO_2 and dissolved inorganic carbon (DIC) during carbonate dissolution, residence time of seepage water, and other chemical and physical conditions (e.g., pH, T) when seepage water passes through bedrock, etc. (Beck et al., 2001; Genty et al., 2001; Hoffmann et al., 2010; Oster et al., 2010; Southon et al., 2012). In some cases, DCF can be relatively constant in some stalagmites (e.g., Southon et al., 2012). Recently, we have found that many stalagmites contain little DCF (e.g., Zhao et al., 2015), so that AMS ^{14}C dating has a potential to build up stalagmite chronology. In Table 2, sample 20140607-1A is the youngest part of the coral reef limestone in Dagangshan Mt. Sample 20140607-1B is residue of a corrupted shell in the coral limestone sample. These two samples have ^{14}C ages of late Pleistocene, much younger than the previously estimated age. Based on tectonic uplift rate, previous studies considered that the age of Dagangshan coral reef limestone was older than 100 ka (Gong et al., 1996, 1998). Although alteration of the coral reef limestone could lead to younger ^{14}C age, further investigation of absolute dating on the coral reef limestone is needed.

Sample 20140607-5 is soda-straw collected from a military cave in the same area. These military caves were excavated after World War II. Therefore, 20140607-5 should be modern. However, the ^{14}C age of this sample is 1295 ± 5 yr BP, showing apparent dead carbon effect. We also collected surface soil and plant in June 2014 near Jianfei Cave to measure ^{14}C ages of organic carbon in the samples. DGM1 (soil) and DGM2 (plant remain) have ^{14}C ages of 675 ± 5 and 625 ± 40 yr BP, respectively. As the plants grow in the limestone area, dead carbon effect can also influence ^{14}C age of the organic carbon. Therefore, we anticipate that the ^{14}C ages of the stalagmite could contain dead carbon effect. In Table 2, all 21 ^{14}C ages in DGS-1 are less than 2800 years old, and the bottom sample has a ^{14}C age of 1850 ± 15 yr BP. Therefore, DGS-1 should be younger than 1900 years even if dead carbon influence exists. In order to understand the dead carbon influence on ^{14}C ages of DGS-1, we plot the $\Delta^{14}C$ [$\Delta^{14}C = (pMC - 1) * 1000‰$, where pMC is fraction modern carbon] with the $\delta^{18}O$ and $\delta^{13}C$ records of DGS-1 (Fig. 6). Fig. 6 exhibits that when the $\delta^{18}O$ and $\delta^{13}C$ values have heavier excursion, the $\Delta^{14}C$ becomes more negative which indicates more DCF. In general, heavier $\delta^{18}O$ and $\delta^{13}C$ in stalagmites grown in monsoonal regions reflect drier climatic condition and less vegetation intensity (Li et al., 2011a,b; Paulsen et al., 2003). Since the vadose zone of Jianfei Cave is very thin (3–5 m) with very porous limestone bedrock, the carbonate bedrock dissolution belongs to an open system (i.e., water in contact with soil air – gas exchange during carbonate dissolution) (Hendy, 1970, 1971). Under such a circumstance, the

DCF influence on stalagmite ^{14}C age could be small. However, as we find that the organic carbon of modern soil and plant remain has a ^{14}C age of 625–675 yr BP, this implies that DIC in seepage water could have an initial ^{14}C age of 600 years, so called reservoir age of soil CO_2. Thus, newly deposited calcite in Jianfei Cave may have a 600-year ^{14}C age even the DCF is zero. During dry periods indicated by heavy $\delta^{18}O$, residence time of seepage water increased which led to DCF increase in DIC due to bedrock dissolution. Less vegetation coverage and low biological activity in soil under dry climates would reduce organic carbon decomposition, so that CO_2 from organic matter became less in seepage water DIC. In contrast, DCF in the DIC would increase, which in turn resulted in $\delta^{13}C$ enrichment and $\Delta^{14}C$ depletion in the stalagmite calcite. Thus, we can see that a $\Delta^{14}C$ depletion generally occurred when the $\delta^{18}O$ and $\delta^{13}C$ values had heavier excursion in Fig. 6.

There are six dates containing minimal dead carbon influence shown in Fig. 6. These six dates could be used for chronological reconstruction. We can theoretically estimate DCF effect on different ^{14}C ages. The DCF in stalagmites can be calculated by the following equation (Genty et al., 2001; Hoffmann et al., 2010):

$$DCF = (1 - {}^{14}C_{stal}/{}^{14}C_{atm}) \times 100\% \qquad (1)$$

where ${}^{14}C_{stal}$ is the initial ^{14}C activity of the stalagmite when calcite precipitates; and ${}^{14}C_{atm}$ is the atmospheric ^{14}C activity at the time of calcite deposition. For samples older than 200 years, "nuclear bomb effect" and "fossil CO_2 dilution effect" since industrial revolution should not be considered (Levin et al., 1980; Suess, 1970). For a simplified calculation, we can ignore the atmospheric ^{14}C variation (Reimer et al., 2013) and focus only on the DCF influence. The ${}^{14}C_{stal}/{}^{14}C_{atm}$ can be considered as pMC under different values of DCF, where age = $-8033 \times Ln$(pMC). When DCF = 0, ${}^{14}C_{stal}/{}^{14}C_{atm} = 1$, and ^{14}C ages are true. If DCF = 1% or 0.01, ${}^{14}C_{stal}/{}^{14}C_{atm} = 0.99$ when the carbonate is formed. Consequently, this new deposited carbonate will have an apparent ^{14}C age of 82 years. If a carbonate sample has 30,000 years age and 1% DCF influence, then its apparent ^{14}C age will be 32,940 years. This means that when initial ^{14}C activity in a sample is lower (older age), DCF influence becomes stronger, so that the difference between apparent ^{14}C age and true age becomes greater. Similarly, we can calculate when DCF is 0.05, 0.1 and so on. The calculated results are plotted in Fig. 9. For a sample with an initial ^{14}C age of 600 years,
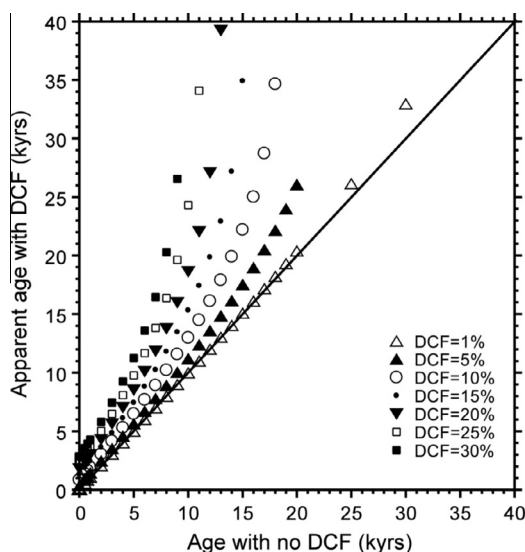
the influence of 15%, 20% and 25% DCF will cause that the apparent ^{14}C ages are 1400, 1930 and 2500 years older, respectively.

In Fig. 10, all ^{14}C dates are plotted with depth. Among the 21 dates, we select the dates with minimal DCF influence by the following criterion: age should be in sequence. Because stalagmite grows upward, from the top to bottom the age is getting older. Therefore, if a date in an upper layer is older than any dates below, this date will not be used. Thus, there are six dates (tri-angle symbols) which meet the above criterion in Fig. 10. The six dates with minimal dead carbon influence can form a linear relationship: Age = (605 ± 70) yr BP + (8.9 ± 0.7) × depth (mm), R^2 = 0.975. This relationship indicates that the top of DGS-1 is 605 yr BP which is very close to the ^{14}C ages of the modern soil and plant remain (Table 2). The fitting also provides a linear growth rate of 0.112 mm/yr. This growth rate is very reasonable for stalagmites in tropical caves. Because the ^{14}C ages of organic carbon in the modern soil and plant remain are 625–675 yr BP and the intercept of the ^{14}C age on the top of the stalagmite is 605 ± 70 yr BP, we need to subtract 600 years from the six selected ^{14}C dates with minimal DCF influence to remove the reservoir age (or DCF influence) completely. In so doing, the top of the stalagmite was AD 1933. When we collected the stalagmite in the field, its surface was dry with no evidence of growth. Since the stalagmite does not show any growth hiatus, we can use the above growth rate to calculate ages for each depths. There six dates (black dots) contain <6% DCF, and other six dates (circles) have DCF of 6–12%. No ^{14}C date excesses 25% DCF. In summary, the AMS ^{14}C dating of DGS-1 provides six ^{14}C ages with minimal dead carbon effect. Using these ages, we are able to build up the chronology of DGS-1. We use linear growth rates between two adjacent ages for calculating age at each depth. The calculation shows that DGS-1 grew from AD 700 to AD 1933. We admit that the chronology is not accurate on annual-to-decadal scales, but it should be reliable on decadal-to-centennial scales.

4.3. $\delta^{18}O$ and $\delta^{13}C$ records of DGS-1

The DGS-1 record has $\delta^{18}O$ values ranging from −10.17‰ to −5.05‰ (VPDB) with an average of −7.37‰ and $\delta^{13}C$ values ranging from −11.63‰ to −4.65‰ with an average of −8.95‰,

Fig. 9. Theoretical calculation of dead carbon effect on ^{14}C ages.

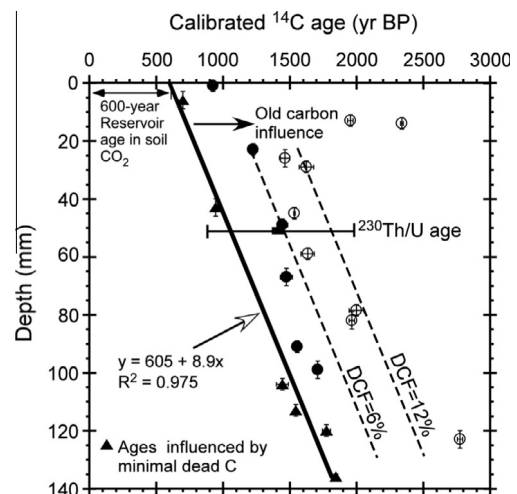**Fig. 10.** Chronology of DGS-1. The ^{14}C dates that have minimal dead carbon influence form a linear line which has an intercept of 605 years. DCF stands for dead carbon fraction. Six dates expressed by solid tri-angles have minimal DCF, which are used for chronological reconstruction. The thick line represents age–depth relationship reconstructed with the six fore-mentioned dates. Six dates shown by black dots have DCF ⩽ 6%, and other dates denoted by open circles have DCF > 6%. Two dashed lines indicate calculated DCF.

respectively. The average growth rate of DGS-1 is 0.112 mm/yr. With 0.1-mm and 0.2-mm sampling intervals, the stable isotope record of DGS-1 has ~1.5-yr resolution. In 2009–2010, we measured δD and $\delta^{18}O$ of cave water in Dagangshan Mt. The average δD and $\delta^{18}O$ values are −39.23‰ (SMOW) and −6.28‰ (SMOW), respectively (Lee, 2010). In the meantime, we also collected rainwater for measuring δD and $\delta^{18}O$ in the study area (Lee, 2010). The δD and $\delta^{18}O$ values of the rainwaters have weighted mean values of −45.02‰ (ranging −110.60‰ to −10.90‰) and −6.63‰ (ranging −13.60‰ to −1.80‰), respectively. The mean $\delta^{18}O$ values of cave water and rainwater are very close, indicating that variation in the $\delta^{18}O$ of cave water reflects change in annually weighted mean $\delta^{18}O$ of rainwater. Since DGS-1 stopped to grow at least 50 years ago, we are not able to use the $\delta^{18}O$ of cave water and cave temperature to check isotopic equilibrium fractionation between calcite and dripping water. However, using mean annual temperature of 23.74 °C and cave water $\delta^{18}O$ of −6.28‰ (SMOW), we obtain −7.73‰ (VPDB) for the $\delta^{18}O$ of calcite under isotopic equilibrium fractionation that is close to the average $\delta^{18}O$ of DGS-1 record. Although Hendy Test (Hendy, 1971) was done on the stalagmite, this classical test has recently been questioned by many researchers (Yin et al., 2014, and references therein). Because we could not find duplicate stalagmites in the cave, therefore we were not able to obtain duplicate $\delta^{18}O$ records. Dorale and Liu (2009) considered that co-variance of $\delta^{18}O$ and $\delta^{13}C$ in a stalagmite could be a better illustration of isotopic equilibrium fractionation. Fig. 6 exhibits similar trends in the $\delta^{18}O$ and $\delta^{13}C$ records of DGS-1, implying that the records represent climatic and environmental changes. The upper 14-mm part of the DGS-1 $\delta^{18}O$ and $\delta^{13}C$ records was compared with lamination bands, showing that the dark bands were corresponding to the heavier $\delta^{18}O$ and $\delta^{13}C$ values (Lee, 2010). It is commonly accepted that in monsoonal regions stalagmite $\delta^{18}O$ registers changes in precipitation amount and $\delta^{18}O$ variation of moisture source in annual-to-decadal scales (Li et al., 1998, 2011a,b; Wan et al., 2011a,b; Yin et al., 2014; Zhao et al., 2015), whereas stalagmite $\delta^{13}C$ can be used for reconstruction of vegetation and climatic conditions on decadal or longer scales (Ku and Li, 1998; Paulsen et al., 2003; Kuo et al., 2011; Li et al., 2012). In general, a light $\delta^{18}O$ and $\delta^{13}C$ excursion in stalagmites on interannual-to-decadal scales reflects a wetter interval with better vegetation coverage; and vice versa.

4.4. Elemental contents of DGS-1

In order to understand chemical compositions of calcite with dark and light colors in DGS-1, we milled three dark layers and three light layers at different depths (Figs. 5 and 7). These powder samples were completely dissolved and analyzed for 23 elements by a PE Optima 7000 ICP-OES. Elements less than 2 mg/kg are ignored, and rest elemental concentrations are listed in Table 3. Since the samples are 99% calcite, Ca concentration needs to be diluted 1 million times in order to be measured by the ICP-OES. Therefore, the uncertainty of Ca measurements could be enlarged by dilution effect. The results in Table 3 indicate that Ca concentrations do not appear apparent differences between adjacent dark and light layers, but concentrations of Mg, Sr, Fe, Mn and Ba in the dark layers are greater than these in the adjacent light layers, especially for Fe and Mn (Table 3). Thus, the ICP-OES results demonstrate that the dark color mainly is caused by impurities of high Fe and Mn contents. In most stalagmites, Fe concentration is normally below 10 mg/kg. However, Fe concentration in DGS-1 reaches as high as 33,000 mg/kg. Interestingly, cave water contains very low Fe. Unlike Mg^{2+}, Sr^{2+}, Ba^{2+} ions which can be easily dissolved in water, dissolved Fe^{2+} and Mn^{2+} exist mainly under reduced conditions. Under oxide condition, Fe^{3+} and Mn^{4+} should become oxides and precipitate quickly. Therefore, how such large

amounts of Fe and Mn got into the stalagmite is unclear. In addition, Sr concentration in DGS-1 is higher than Mg concentration, reflecting contribution of coral reef bedrock. In most limestone caves except dolomite limestone areas, Mg content in stalagmites is one order magnitude higher than Sr content (Li et al., 2006). The reasons of Sr/Mg > 1 in DGS-1 may include: high Sr content in the coral reef limestone and thin overlying soil layer.

Although ICP-OES method can provide absolute concentrations for elements, this method consumes samples and time so that it is difficult to produce continuously high-resolution profiles of elemental variations. With an iTRAX XRF scanner, we are able to obtain relative variability of many elements in stalagmites quickly (Finné et al., 2014). However, few attempts have been done on XRF scan of stalagmites, so that the scanning results have not been understood well yet. As each element has different sensitivity to the XRF scan method and calibration for each element depends on matrix and surface features of samples, quantitatively analysis of XRF scanning for stalagmites has not been established yet. Here we set up two criteria for the reliable XRF scanning results: (1) elemental content should be significantly higher than background; and (2) strongly linear correlation of duplicated runs between two parallel tracks. Among 18 fore-mentioned elements, only 9 elements meet the above criteria. The mean intensities of these elements and their duplicate correlation coefficients are listed in Table 4. Although the correlation coefficient of Si analysis is not high, the variation trends of Si in two tracks are similar (Fig. 7). In general, Si and Ti are mainly from detritus. These two elements co-vary apparently in low resolution (5-point running). Detailed examination on Zn, Cu and Ni profiles show no correlations among these elements, but variations of Zn follow that of Si. Therefore, we select Si profile as detrital background to compare with other profiles (Fig. 7).

Since the iTRAX XRF scanner cannot measure Mg, the other non-Ca elements are Sr, Fe and Mn (Tables 3 and 4). The XRF scanning results of Ca, Sr, Fe and Mn are very reliable shown by strong correlation coefficients ($R^2 > 0.93$). The Fe and Mn profiles strongly co-vary (Fig. 8), indicating similar behavior of the two elements from source to the stalagmite. In Fig. 7, peaks of Fe and Sr are corresponding to peaks of Si, reflecting that Sr and Fe increased when detritus increased. Ca content decreased when Sr and Fe increased. From Figs. 7 and 8, some observations can be done: (1) the dark layers contain higher Fe and Mn because Fe oxides and Mn oxides have dark colors. (2) When detrital content increases shown by increased Si and Ti, the Sr, Fe and Mn contents in the stalagmite are also higher. (3) Carbonate content was decreased during the peaks of Sr, Fe and Mn, implying that when calcite deposited at lower rate, detritus and impurities in the stalagmite would increase via dust fall and/or seepage flow. (4) Since the dark layers are mainly correlated with heavier $\delta^{18}O$ and $\delta^{13}C$ values as discussed before, peaks of Fe and Mn reflect dry/hot climatic conditions. (5) The upper 60 mm of DGS-1 contained low Fe except three peaks between 40 mm and 55 mm depths, whereas very high Fe contents appeared between 65 mm and 75 mm depths. In general, warm condition is in favor of Fe oxide formation. During dry intervals, the residence time of seepage water increased so that water–rock interaction increased, resulting in more dissolved Fe, Mn and Sr from soil and bedrock. If temperature kept low, Fe and Mn would remain in dissolved phase as Fe^{2+} and Mn^{2+} formats. Under warm conditions, these dissolved Fe and Mn became oxides to precipitate in the stalagmite. Hence, Fe and Mn peaks in DGS-1 might represent warm but dry climates. (6) High Sr but low Ca below 120 mm depth probably indicates larger contribution of dissolution from coral reef limestone during the early formation of the stalagmite. When seepage water contained too much salt dissolved from the overlying sediments which initially deposited in marine environment, it was difficult to precipitate calcite and to form

stalagmites. In summary, peaks of Sr, Fe and Mn in DGS-1 reflect dry intervals, and peaks of Fe and Mn correlate with dark color layers which deposited under warm episodes.

5. Climatic forcing of rainfall in South Taiwan on interannual and decadal scales

Based on the current chronology, $\delta^{18}O$, $\delta^{13}C$ and Fe content of Stalagmite DGS-1, we compare the records with other climatic records and discuss the climatic patterns and forcing factors. First of all, we compare the $\delta^{18}O$ of DGS-1 with the East Asia Summer Monsoon index (using 5-yr running average) published by IPCC (2007) and Tainan rainfall (5-yr running average) to examine the physical meaning of the $\delta^{18}O$ record (Fig. 11). Within age uncertainties of the DGS-1 $\delta^{18}O$ record, the comparison in Fig. 11 clearly demonstrates that under stronger EASM climatic condition in the study area, the annual rainfall and summer rainfall in Tainan are higher, and the $\delta^{18}O$ becomes lighter. Therefore, we consider that a negative swing in the DGS-1 $\delta^{18}O$ record indicates stronger EASM and wetter climate on decadal scales. Note that variations in Tainan rainfall do not have one-to-one correlation with changes in the EASM strength, implying that other forcings affect the rainfall. The above comparison illustrates that the chronology of DGS-1 is reliable on decadal or longer scales.

The DGS-1 record covers periods of the Little Ice Age (LIA, AD 1300–1850) and the Medieval Warm Period (MWP, AD 900–1100) (Fagan, 2000; Ledru et al., 2013). For the LIA, many previous studies have found that there are two phases in the LIA with different climatic patterns (e.g., Chu et al., 2012; Paulsen et al., 2003; Shen et al., 2006; Wan et al., 2011b; Wang et al., 2013, 2014a,c; Yin et al., 2014). Although the climatic conditions during MWP and LIA may have spatial variations and the time definition may be location dependent, the temperature conditions for those periods are generally known. According to $\delta^{18}O$, $\delta^{13}C$ and Fe records of Stalagmite DGS-1, we may classify five periods with different climatic regimes and environmental conditions during AD 700–AD 1930 in the study area (Fig. 12). Period I: AD 700–AD 1200. Climate during this period was wet and relatively warm, reflected by lighter-than-average $\delta^{18}O$ and $\delta^{13}C$, and moderate Fe contents. The $\delta^{18}O$ and $\delta^{13}C$ had heaviest values around AD 1050 during

Period I, which was corresponding to the Oort Minimum in solar activity marked as E in Fig. 12. The total solar irradiation during this period was generally high and Sunspot numbers reached Medieval Maximum around AD 1100 (Solanki et al., 2004; Steinhilber et al., 2009). The Fe content was low corresponding to the Oort Minimum and was high corresponding to high solar activities before and after the Oort Minimum (Fig. 12). Low Fe contents AD 800 and AD 950 might be due to wet climatic conditions shown by light $\delta^{18}O$ values, so that temperature influence became minor. Period II: AD 1200–AD 1400. The $\delta^{18}O$ had a general enrichment trend from AD 1200 toward late AD 1300s. Both $\delta^{18}O$ and $\delta^{13}C$ reached the heaviest values of Period II around AD 1360, perhaps corresponding to the Wolf Minimum around AD 1300 (Marked as D in Fig. 12). However, a 50-year leg exists between the heaviest $\delta^{18}O$ and $\delta^{13}C$ values and the Wolf Minimum. Whether this time leg was due to age uncertainty or climatic and environmental response is unclear. Evaluating the Fe content of this period shows that low Fe was corresponding to the Wolf Minimum in the TSI record, and high Fe matches high TSI before and after the Wolf Minimum. Note that the oceanic condition was turned from an El Niño-like state to a La Niña-like state shown by SOI record in Fig. 12 (Oppo et al., 2009; Yan et al., 2011b). It is possible that switch in the oceanic condition might disrupt the strong correlation between solar activity and EASM strength. At the interval of the maximum Fe peaks, the climatic condition was dry and vegetation was poor indicated by the heaviest $\delta^{18}O$ and $\delta^{13}C$, the temperature was not cold reflected by the TSI record. Consequently, Fe oxide could have the best conditions to be deposited. Period III (The Little Ice Age Phase I): AD 1400–AD 1610. Solar activity during this period strongly decreased since AD 1370 and reached minimum around AD 1460, as known as Spörer Minimum (Marked as C). The $\delta^{18}O$ of DGS-1 was strongly enriched following the solar activity. It is interesting to see that the $\delta^{18}O$ and $\delta^{13}C$ co-varied well on interannual-to-decadal scales, but the $\delta^{18}O$ values were below (heavier than) the $\delta^{18}O$ average while the $\delta^{13}C$ values were above (lighter than) the $\delta^{13}C$ average (Fig. 12). This means that the climatic condition during Period III was not dry reflected by the $\delta^{13}C$ record even though the $\delta^{18}O$ values were relatively heavy. The phenomenon of heavier-than- average $\delta^{18}O$ values of this period might be caused by heavier $\delta^{18}O$ value in the
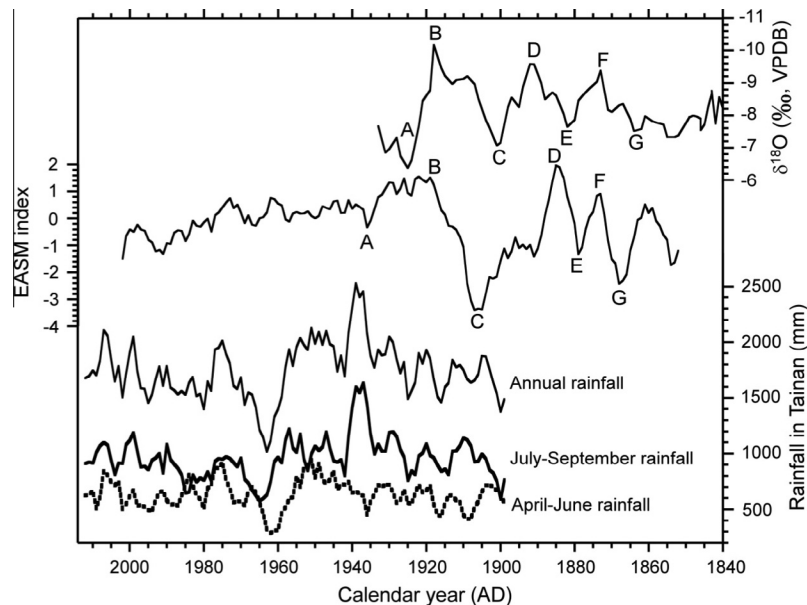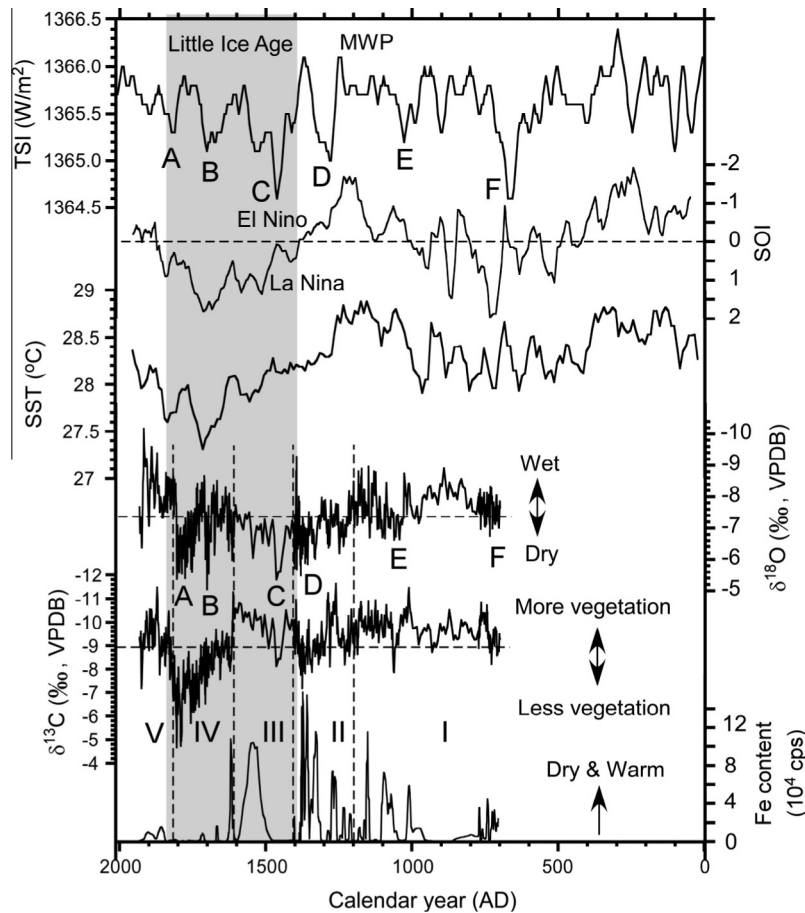

Fig. 11. Comparison of the DGS-1 $\delta^{18}O$ record with the 5-yr running averages of EASM index (IPCC, 2007) and Tainan rainfall. The letters denote possible corresponding events.

Fig. 12. Comparisons of the $\delta^{18}O$, $\delta^{13}C$ and Fe records in DGS-1 with SST of the Indo-Pacific warm pool (Oppo et al., 2009), Southern Oscillation Index (Yan et al., 2011b), and Total solar irradiation (Delaygue and Bard, 2011). The horizontal dashed lines denote the average values of each parameter. The vertical dashed lines separate major climatic regimes shown by Roma letters based on isotopic and geochemical features of DGS-1. The capital letters indicate possible corresponding events.

moisture source. During this period, ITCZ migrated northward (Yan et al., 2011a), probably brought up more southerly moisture with heavy $\delta^{18}O$. In the Dahu Lake record of NE Taiwan, wet and stable climatic conditions were prevailing during the Little Ice Age phase 1 (LIA 1 – AD 1400–1620) (Wang et al., 2014a; Yang et al., 2014). The Fe content was low corresponding to the Spörer Minimum, turned to high following the solar irradiation increase. It is understandable that when climate was not so dry, temperature would dominate Fe oxide precipitation, with colder temperature (during the Spörer Minimum) depositing less Fe oxide; and vice versa. Therefore, we conclude that climate during Period III should be relatively wet with good vegetation coverage in the study area. Period IV (The Little Ice Age Phase II): AD 1610–AD 1810. The $\delta^{18}O$ of DGS-1 was strongly fluctuated and relatively heavy even though the ITCZ shifted southward since AD 1600 (Yan et al., 2011a). Two heavy $\delta^{18}O$ excursions were corresponding to the Maunde Minimum (Marked as B) and Dalton Minimum (Marked as A), respectively. The $\delta^{13}C$ values were much heavier than the average $\delta^{13}C$ and reached the maximum value during the Dalton Minimum. The study area had dry and cold climate conditions with poor vegetation coverage during Period IV corresponding to the Little Ice Age Phase II. Low Fe content during this period was probably attributed to the cold temperature. Biological activity in soil could be weak under dry and cold condition, resulting in less dissolution of Fe from detritus. Dissolved Fe would keep Fe^{2+} under cold temperature, so that Fe oxide was not easy to form. The oceanic condition was mainly in strong La Niña-like state during Period

IV (Yan et al., 2011b), implying that precipitation in South Taiwan could be low in La Nina-like state. In NE Taiwan, the Dahu Lake record indicates dry and more dynamic climates during the same period (Wang et al., 2014a; Yang et al., 2014). Period V (Current Warm Period): AD 1810–AD 1933. Since AD 1810, both $\delta^{18}O$ and $\delta^{13}C$ of DGS-1 were strongly depleted, reached the conditions similar to Period I. Warm and wet climates with abundant vegetation intensity were dominant in the study area during Period V. The $\delta^{18}O$ values between AD 1300 and AD 1800 of DGS-1 were mainly heavier than the average value (Fig. 12), reflecting weak summer monsoon. This weak summer monsoon period was corresponding to the LIA well, which agreed generally with the Great Ghost Lake record that showed a major dry period of 50–550 yr BP (ca. AD 1400–AD 1900) (Wann, 2000).

The comparisons in Figs. 3, 4, 11 and 12 illustrate that rainfall in South Taiwan on interannual to decadal scales is influenced by Solar activity, the EASM strength, ITCZ shift, ENSO-like and PDO oceanic conditions. However, the influences of solar activity and oceanic condition on rainfall in South Taiwan are different on decadal or centennial scales, and also different from other regions in eastern China. On decadal-to-multi decadal scales, increase in total solar irradiation (TSI) leads to an increased temperature in North Hemisphere which results in an enhanced EASM strength. Consequently, climate in South Taiwan is wet. During all Sunspot minima over the last millennium, climates in the study area were dry (Fig. 12). On decadal or longer scales, El Niño-like condition and warm PDO phase are in favor of wet climate in South

Taiwan (Figs. 3 and 12). This situation is different in the monsoonal region of Eastern China where wet climate is corresponding to La Niña-like condition and cold PDO phase (e.g., Yin et al., 2014; Zhao et al., 2015). In fact, Wann (2000) discussed the differences of rainfall variations between South Taiwan and the monsoonal region in eastern China as fore-mentioned. According to modern precipitation data base, a strong summer monsoon may produce positively rainfall anomaly in north and south China, but negatively rainfall anomaly in low-mid Yangtze River drainage Basin; and vice versa (Guo et al., 2003; Zhang et al., 2010). In addition, on centennial scales, warm N. Hemisphere condition during the Medieval Warm Period (WMP) was correlated with an El Niño-like state and a strong EASM phase, while cold N. Hemisphere condition during the Little Ice Age (LIA) gave opposite correlations (Yan et al., 2011b) (Fig. 12). It is clear that climatic forcing factors have different dominant controls on different time scales. Therefore, one should evaluate the effect of EASM strength on precipitation in different regions and different time scales.

6. Conclusions

Stalagmite DGS-1 from Dagangshan Mountain of South Taiwan was dated by AMS ^{14}C dating, spanning a depositional record from AD 700 to AD 1933. Continuous, high-resolution δ^{18}O and δ^{13}C records and XRF scan elemental profiles reveal interannual-to-decadal variations in climate and environmental conditions. The comparison of the δ^{18}O record with instrumentally recorded EASM index proves not only the chronology of the DGS-1, but also physical meaning of the δ^{18}O record with lighter δ^{18}O corresponding to stronger EASM and high rainfall. High Fe, Mn and Sr contents from detritus and bedrocks were deposited during relatively dry episodes to form dark layers of Stalagmite DGS-1. Fe and Mn contents representing Fe and Mn oxides vary with both hydrological condition and temperature, being dry and warm in favor of the oxide precipitation. The DGS-1 record exhibits five periods with different climate regimes and vegetation conditions: Period I (AD 700–1200), warm and wet climates with good vegetation coverage; Period II (AD 1200–1400), climate turned to dry and vegetation became less abundant. The oceanic condition was switching from an El Niño-like state to a La Niña-like state at the end of this period. Period III (AD 1400–1610) corresponding to the LIA phase I, cold but relatively wet climates with good vegetation coverage were prevailing in the study area. Period IV (AD 1610–1810) corresponding to the LIA phase II, cold and dry climates with poor vegetation coverage were dominant in the study area. Period V (AD 1810–1933), climate turned warm and wet and vegetation resumed similar to Period I. Based on the 117-yr Tainan rainfall record, we found that enhanced southwesterly rains (AMJ rainfall) correspond weak EASM, El Niño condition, warm PDO phase and increased winter branch of KC on interannual variability; and strong EASM, La Niña condition and cold PDO phase can generally produce higher JAS rainfall but lower AMJ rainfall. Study of correlation between ENSO and rainfall should be carried out on seasonal scale. On interannual-to-decadal scales, solar activity is the dominant factor to influence precipitation in South Taiwan, stronger TSI resulting in wet climate under an increased EASM strength; and vice versa. On decadal-to-centennial scales, strong El Niño-like state and warm PDO phase are in favor of wet conditions in South Taiwan; and vice versa. Such situations are different from some monsoonal regions in Eastern China.

Acknowledgements

References

Allan, R.J., Nicholls, N., Jones, P.D., Butterworth, I.J., 1991. A further extension of the Tahiti-Darwin SOI, early SOI results and Darwin pressure. J. Clim. 4, 743–749.

Beck, J.W., Richards, D.A., Edwards, R.L., Silverman, B.W., Smart, P.L., Donahue, D.J., Hererra-Osterheld, S., Burr, G.S., Calsoyas, L., Jull, A.J.T., Biddulph, D., 2001. Extremely large variations in atmospheric C-14 concentration during the last glacial period. Science 292, 2453–2458.

Chen, H.-F., Wen, S.-Y., Song, S.-R., Yang, T.-N., Lee, T.-Q., Lin, S.-F., Hsu, S.-C., Wei, K.-Y., Chang, P.-Y., Yu, P.-S., 2012. Strengthening of paleo-typhoon and autumn rainfall in Taiwan corresponding to the Southern Oscillation at late Holocene. J. Quatern. Sci. 27, 964–972.

Chen, S.H., Wu, J.T., 1999. Paleolimnological environment indicated by the diatom and pollen assemblages in an alpine lake in Taiwan. J. Paleolimnol. 22, 149–158.

Chen, S.-H., Wu, J.-T., Yang, T.-N., Chuang, P.-P., Huang, S.-Y., Wang, Y.-S., 2009. Late Holocene paleoenvironmental changes in subtropical Taiwan inferred from pollen and diatoms in lake sediments. J. Paleolimnol. 41, 315–327.

Cheng, H., Edwards, R.L., Hoff, J., Gallup, C.D., Richards, D.A., Asmersom, Y., 2000. The half-lives of uranium-234 and thorium-230. Chem. Geol. 169, 17–33.

Cook, E.R., D'Arrigo, R.D., Anchukaitis, K.J., 2008. ENSO reconstructions from long tree-ring chronologies: unifying the differences. In: Talk Presented at a Special Workshop on Reconciling ENSO Chronologies for the Past 500 Years, held in Moorea, French Polynesia on 2–3 April 2008.

Chu, P.-C., Li, H.-C., Fan, C.-W., Chen, Y.-H., 2012. Speleothem evidence for temporal-spatial variation in East Asian summer monsoon since medieval warm period. J. Quat. Sci. 27 (9), 901–910.

Delaygue, G., Bard, E., 2011. An Antarctic view of Beryllium-10 and solar activity for the past millennium. Clim. Dyn. 36, 2201–2218.

Dorale, J.A., Liu, Z.-H., 2009. Limitations of Hendy test criteria in judging the paleoclimatic suitability of speleothems and the need for replication. J. Cave Karst Study 71, 73–80.

Elsner, J.B., Liu, K.B., 2003. Examining the ENSO-typhoon hypothesis. Clim. Res. 25, 43–54.

Enfield, D.B., Mestas-Nuñez, A.M., 1999. Multiscale variabilities in global sea surface temperatures and their relationship with tropospheric climate patterns. J. Clim. 12, 2719–2733.

Fagan, B.M., 2000. The Little Ice Age: How Climate Made History, 1300–1850. New York: Basic Books, xxi and 246 pp. (ISBN 0-465-02271-5).

Finné, M., Kylander, M., Boyd, M., Sundqvist, H.S., Löwemark L., 2014. Can XRF scanning of speleothems be used as a non-destructive method to identify paleoflood events in caves? Int. J. Speleol., 44 (1), 17–23. Tampa, FL (USA) ISSN 0392–6672 http://dx.doi.org/10.5038/1827-806X.44.1.2.

Guo, Q.Y., Cai, J.N., Shao, X.M., Sha, W.Y., 2003. Interdecadal variability of East-Asian summer monsoon and its impact on the climate of China. Acta Geographica Sinica 4, 569–576 (in Chinese).

Genty, D., Baker, A., Massault, M., Proctor, C., Gilmour, M., Pons-Branchu, E., Hamelin, B., 2001. Dead carbon in stalagmites: carbonate bedrock paleodissolution vs. ageing of soil organic matter. Implications for ^{13}C variations in speleothems. Geochim. Cosmochim. Acta 65, 3443–3457.

Gong, S.Y., Lee, T.Y., Wu, J.C., Wang, S.W., Yang, K.M., 1996. Possible links between the development of Plio-Pleistocene coral reef limestones and thrust migration in southwestern Taiwan. J. Geol. Soc. China 39, 151–160.

Gong, S.Y., Wang, S.W., Lee, T.Y., 1998. Pleistocene coral reefs associated with claystones, Southwestern Taiwan. Coral Reefs 17, 215–222.

Hendy, C.J., 1970. The use of ^{14}C in the study of cave processes. In: Almqvist, Wiksell (Ed.), Nobel Symposium 12. Radiocarbon Variations and Absolute Chronology, Stockholm.

Hendy, C.H., 1971. The isotopic geochemistry of speleothems—I. The calculation of the effects of different modes of formation on the isotopic composition of speleothems and their applicability as paleoclimate indicators. Geochim. Cosmochim. Acta 35, 801–824.

Hoffmann, D.L., Beck, J.W., Richards, D.A., Smart, P.L., Singarayer, J.S., Ketchmark, T., Hawkesworth, C.J., 2010. Towards radiocarbon calibration beyond 28 ka using speleothems from the Bahamas. Earth Planet. Sci. Lett. 289, 1–10.

Hu, J.Y., Kawamura, H., Hong, H.S., Qi, Y.Q., 2000. A review on the currents in the South China Sea: seasonal circulation, South China Sea warm current and Kuroshio intrusion. J. Oceanogr. 57, 607–624.

IPCC, 2007. Climate Change 2007 – the physical science basis. In: Solomon, S., Qin, D., Manning, M., Chen, Z., Marquis, M., Averyt, K.B., Tignor, M., Miller, H.L. (Eds.), Contribution of Working Group I to the Fourth Assessment Report of the Intergovernmental Panel on Climate Change. Cambridge University Press, Cambridge, United Kingdom and New York, NY, USA, p. 996.

Ku, T.-L., Li, H.-C., 1998. Speleothems as high-resolution paleoenvironment archives: records from northeastern China. J. Earth Syst. Sci. 107, 321–330.

Kuo, T.-S., Liu, Z.-Q., Li, H.-C., Wan, N.-J., Shen, C.-C., Ku, T.-L., 2011. Climate and environmental changes during the past millennium in central western Guizhou reflected by Stalagmite ZJD-21 record. J. Asian Earth Sci. 40, 1111–1120.

Ledru, M.-P., Jomelli, V., Samaniego, P., Vuille, M., Hidalgo, S., Herrera, M., Ceron, C., 2013. The medieval climate anomaly and the Little Ice Age in the eastern Ecuadorian Andes. Clim. Past 9, 307–321.

Lee, Z.-Z., 2010. Depositional Features of Stalagmite DGS-01 from a Limestone Cave in Dagangshan, Kaohsiung. National Cheng-Kung University of Taiwan. MS thesis. 72p (in Chinese).

Levin, I., Munnich, K., Weiss, W., 1980. The effect of anthropogenic CO_2 and ^{14}C sources on the distribution of ^{14}C in the atmosphere. In: Stuiver, M., Kra, R.S., (Eds.), The 10th International ^{14}C conference Proceedings: Radiocarbon 22, pp. 379–391.

Li, H.-C., Ku, T.-L., Stott, L.D., Chen, W.J., 1998. Applications of interannual -resolution stable isotope records of speleothem: climatic changes in Beijing and Tianjin, China during the past 500 years — the $\delta^{18}O$ record. Sci. China 41, 362–368.

Li, H.-C., Lee, Z.-H., Wan, N.-J., Shen, C.-C., Li, T.Y., Yuan, D.X., Chen, Y.H., 2011a. Interpretations of $\delta^{18}O$ and $\delta^{13}C$ in aragonite stalagmites from Furong Cave, Chongqing, China: a 2000-year record of monsoonal climate. J Asia Earth Sci 40, 1121–1130.

Li, H.-C., Liew, P.-M., Seki, O., Kuo, T.-S., Kawamura, K., Wang, L.-Q., Lee, T.-Q., 2013. Paleoclimate variability in central Taiwan during the past 30 ka reflected by pollen, TOC, $\delta^{13}C_{TOC}$, and n-alkane- δD records in a peat sequence from Toushe Basin. J. Asian Earth Sci. 69, 185–195.

Li, J.-Y., Li, H.-C., Liu, Z.-Q., Yuan, D.X., He, X., Wang, R.M., 2006. Geochemistry features and Mg/Sr ratios of water and speleothem samples from caves in central western Guizhou, China. Carsologica Sinica 25, 177–186 (In Chinese).

Li, T.-Y., Shen, C.-C., Li, H.-C., Li, J.-J., Chiang, H.-W., Song, S.-R., Yuan, D.-X., Lin, Chris D.-J., Gao, P., Zhou, L.-P., Wang, J.-L., Ye, M.-Y., Tang, L.-L., 2011b. Oxygen and carbon isotopic systematics of aragonite speleothems and water in Furong Cave, Chongqing, China. Geochim. Cosmochim. Acta 75, 4140–4156.

Li, T.-Y., Li, H.-C., Xiang, X.-J., Kuo, T.-S., Li, J.-Y., Zhou, F.-L., Chen, H.-L., Peng, L.-L., 2012. Transportation characteristics of $\delta^{13}C$ in the plants-soil-bedrock -cave system in Chongqing karst area. Science in China (D) 55, 685–694. http://dx.doi.org/10.1007/s11430-011-4294-y.

Liew, P.-M., Lee, C.-Y., Kuo, C.-M., 2006a. Holocene thermal optimal and climate variability of East Asian monsoon inferred from forest reconstruction of a subalpine pollen sequence, Taiwan. Earth Planetary Sci. Lett. 250, 596–605.

Liew, P.-M., Huang, S.-Y., Kuo, C.-M., 2006b. Pollen stratigraphy, vegetation and environment of the last glacial and Holocene—a record from Toushe Basin, central Taiwan. Quatern. Int. 147, 16–33.

Lo, J.-Y., Chen, C.T.A., Wann, J.-K., 1996. Paleoclimate study of the Great Ghost Lake in Taiwan. Sci. China (D) 26 (5), 474–480 (in Chinese).

Mantua, N.J., Hare, S.R., Zhang, Y., Wallace, J.M., Francis, R.C., 1997. A Pacific interdecadal climate oscillation with impacts on salmon production. Bull. Am. Meteorol. Soc. 78, 1069–1079.

Olesik, J.W., 1991. Elemental analysis using ICP-OES and ICP/MS. Anal. Chem. 63 (1), 12A–21A.

Oppo, D.W., Rosenthal, Y., Linsley, B.K., 2009. 2000-year-long temperature and hydrology reconstructions from the Indo-Pacific warm pool. Nature 460, 1113–1116. http://dx.doi.org/10.1038/nature08233.

Oster, J.L., Montañez, I.P., Gulderson, T.P., Sharp, W.D., Banner, J.L., 2010. Modeling speleothem $\delta^{13}C$ variability in a central Sierra Nevada cave using ^{14}C and $^{87}Sr/^{86}Sr$. Geochim. Cosmochim. Acta 74, 5228–5242.

Paulsen, D.E., Li, H.-C., Ku, T.-L., 2003. Climate variability in central China over the last 1270 years revealed by high-resolution stalagmite records. Quatern. Sci. Rev. 22, 691–701.

Qiu, B., 2001. Kuroshio and Oyashio currents. In: Encyclopedia of Ocean Sciences. Academic Press, pp. 1413–1425.

Qiu, B., 2002. The Kuroshio extension system: its large-scale variability and role in the midlatitude ocean-atmosphere interaction. J. Oceanogr. 58, 57–75.

Qu, T.-D., Kim, Y.Y., Yaremchuk, M., 2004. Can Luzon Strait transport play a role in conveying the impact of ENSO to the South China Sea? J. Clim. 17, 3644–3657.

Reimer, P.J., Bard, E., Bayliss, A., Beck, J.W., Blackwell, P.G., Ramsey, C.B., Buck, C.E., Cheng, H., Edwards, R.L., Friedrich, M., Grootes, P.M., Guilderson, T.P., Haflidason, H., Hajdas, I., Hatté, C., Heaton, T.J., Hoffmann, D.L., Hogg, A.G., Hughen, K.A., Kaiser, K.F., Kromer, B., Manning, S.W., Niu, M., Reimer, R.M., Richards, D.A., Scott, E.M., Southon, J.R., Staff, R.A., Turney, C.S.M., van der Plicht, J., 2013. IntCal13 and Marine13 radiocarbon age calibration curves 0–50,000 years cal BP. Radiocarbon 55, 1869–1887.

Shen, C.-C., Edwards, R.L., Cheng, H., Dorale, J.A., Thomas, R.B., Moran, S.B., Weinstein, S.E., 2002. Uranium and thorium isotopic and concentration measurements by magnetic sector inductively coupled plasma mass spectrometry. Chem. Geol. 185, 165–178.

Shen, C.-C., Cheng, H., Edwards, R.L., Moran, S.B., Edmonds, H.N., Hoff, J.A., Thomas, R.B., 2003. Measurement of attogram quantities of ^{231}Pa in dissolved and particulate fractions of seawater by isotope dilution thermal ionization mass spectroscopy. Anal. Chem. 75, 1075–1079.

Shen, C.M., Wei-Chyung Wang, W.-C., Gong, W., Hao, Z.X., 2006. A Pacific Decadal Oscillation record since 1470 AD reconstructed from proxy data of summer rainfall over eastern China. Geophys. Res. Lett. 33, L03702. http://dx.doi.org/10.1029/2005GL024804.

Shen, C.-C., Wu, C.-C., Cheng, H., Edwards, R.L., Hsieh, Y.-T., Gallet, S., Chang, C.-C., Li, T.-Y., Lam, D.D., Kano, A., Hori, M., Spötl, C., 2012. High-precision and high-resolution carbonate ^{230}Th dating by MC-ICP-MS with SEM protocols. Geochim. Cosmochim. Acta 99, 71–86.

Solanki, S.K., Usoskin, I.G., Kromer, B., Schüssler, M., Beer, J., 2004. An unusually active Sun during recent decades compared to the previous 11,000 years. Nature 431 (7012), 1084–1087.

Southon, J., Noronha, A.L., Cheng, H., Edwards, R.L., Wang, Y.J., 2012. A high-resolution record of atmospheric ^{14}C based on Hulu Cave speleothem H82. Quatern. Sci. Rev. 33, 32–41.

Steinhilber, F., Beer, J., Fröhlich, C., 2009. Total solar irradiance during the Holocene. Geophys. Res. Lett. 36, L19704. http://dx.doi.org/10.1029/2009GL040142.

Stuiver, M., Reimer, P.J., 1986. A computer program for radiocarbon age calibration. Radiocarbon 28 (2B), 1022–1030.

Stuiver, M., Reimer, P.J., 1993. Extended ^{14}C data base and revised CALIB 3.014 C age calibration program. Radiocarbon 35, 215–230.

Suess, H.E., 1970. The three causes of the secular C-14 fluctuations, their amplitudes and time constants. In: Olsson, I.U., (Ed.), Radiocarbon variations and absolute chronology, Nobel symposium, 12th, Proc: New York, John Wiley and Sons, p. 595–612.

Trenberth, K.E., 1997. The definition of El Niño. Bull. Am. Meteorol. Soc. 78, 2771–2777.

Trenberth, K.E., Hurrell, J.W., 1994. Decadal atmosphere-ocean variations in the Pacific. Clim. Dyn. 9, 303–319.

Tsou, C.-Y., Feng, Z.-Y., Chigira, M., 2011. Catastrophic landslide induced by Typhoon Morakot, Shiaolin, Taiwan. Geomorphology 127, 166–178.

Tsukada, M., 1966. Late Pleistocene vegetation and climate in Taiwan (Formosa). Proc. Natl. Acad. Sci. USA 55, 543–548.

Wan, N.-J., Chung, W.-L., Li, H.-C., Lin, H.L., Shen, C.-C., Ku, T.-L., Yuan, D.X., Zhang, M.L., Lin, Y.S., 2011a. The comparison of speleothem $\delta^{18}O$ records from Eastern China with solar insolation, ice core and marine records: similarities and discrepancies on different time scales. J. Asia Earth Sci. 40, 1151–1163.

Wan, N.-J., Li, H.-C., Liu, Z.Q., Yuan, D.X., 2011b. Spatial variations of monsoonal rain in eastern China: instrumental, historic and speleothem records. J. Asia Earth Sci. 40, 1139–1150.

Wang, B., Wu, R.G., Fu, X.H., 2000. Pacific-East Asian teleconnection: how does ENSO affect East Asian climate? J. Clim. 13, 1517–1536.

Wang, B., Wu, R.G., Lau, K.-M., 2001. Interannual variability of the Asian summer monsoon: contrasts between the Indian and the Western North Pacific-East Asian Monsoons. J. Clim. 13, 4073–4090.

Wang, L.-C., Behling, H., Lee, T.-Q., Li, H.-C., Huh, C.-A., Shiau, L.-J., Chang, Y.-P., 2014a. Late Holocene environmental reconstructions and their implications on flood events, typhoon, and agricultural activities in NE Taiwan. Clim. Past 10, 1857–1869. http://dx.doi.org/10.5194/cp-10-1857-2014.

Wang, L.-C., Behling, H., Chen, Y.-M., Huang, M.-S., Chen, C.T., Lo, J.-Y., Chang, Y.-P., Li, H.-C., 2014b. Holocene monsoonal climate changes tracked by multiproxy approach from a lacustrine sediment core of the subalpine Retread Lake in Taiwan. Quatern. Int. 333, 69–76.

Wang, L.-C., Behling, H., Lee, T.-Q., Li, H.-C., Huh, C.-A., Shiau, L.-J., Chang, Y.-P., 2014c. Late Holocene environmental reconstructions and the implications on flood events, typhoon patterns, and agriculture activities in NE Taiwan. Clim. Past 10, 1857–1860.

Wang, L.-C., Behling, H., Lee, T.-Q., Li, H.-C., Huh, C.-A., Shiau, L.-J., Chen, S.-H., Wu, J.-T., 2013. Increased precipitation during the Little Ice Age in northern Taiwan inferred from diatoms and geochemistry in a sediment core from a subalpine lake. J. Paleolimnol. 49, 513–535.

Wann, J.-K., 2000. Geochemistry and paleoclimate of the seasonally anoxic Great Ghost Lake. PhD Thesis. National Sun Yat-sen University of Taiwan, 205p (in Chinese).

Woodruff, J.D., Donnelly, J.P., Okusu, A., 2009. Exploring typhoon variability over the mid-to-late Holocene: evidence of extreme coastal flooding from Kamikoshiki, Japan. Quatern. Sci. Rev. 28, 1774–1785.

Yan, H., Sun, L., Oppo, D.W., Wang, Y., Liu, Z., Xie, Z., Liu, X., Cheng, W., 2011a. South China Sea hydrological changes and Pacific Walker Circulation variations over the last millennium. Nat. Commun. 2, 293.

Yan, H., Sun, L., Wang, Y.-H., Huang, W., Qiu, S.-C., Yang, C.-Y., 2011b. A record of the Southern Oscillation Index for the past 2000 years from precipitation proxies. Nat. Geosci. 4, 611–614.

Yang, T.-N., Lee, T.-Q., Meyers, P.A., Song, S.-R., Kao, S.-J., Löwemark, L., Chen, R.-F., Chen, H.-F., Wei, K.-Y., Fan, C.-W., Shiau, L.-J., Chiang, H.-W., 2011. Variations in monsoonal rainfall over the last 21 kyr inferred from sedimentary organic matter in Tung-Yuan Pond, southern Taiwan. Quatern. Sci. Rev. 30, 3413–3422.

Yang, T.-N., Lee, T.-Q., Lee, M.-Y., Huh, C.-A., Meyers, P.A., Löwemark, L., Wang, L.-Q., Kao, W.-Y., Wei, K.-Y., Chen, R.-F., Chen, H.-F., Chen, S.-H., Wu, J.-T., Shiau, L.-J., Chen, Y.-G., Hsieh, Y.-C., 2014. Paleohydrological changes in northeastern Taiwan over the past 2 ky inferred from biological proxies in the sediment record of a floodplain lake. Palaeogeogr. Palaeoclimatol. Palaeoecol. 410, 401–411.

Yang, T.-N., Lee, T.-Q., Meyers, P.A., Fan, C.-W., Chen, R.-F., Wei, K.-Y., Chen, Y.-G., Wu, J.-T., 2013. The effect of typhoon induced rainfall on settling fluxes of particles and organic carbon in Yuanyang Lake, subtropical Taiwan. J. Asian Earth Sci. 40, 1171–1179.

Yin, J.J., Yuan, D.X., Li, H.-C., Cheng, H., Li, T.Y., Edwards, R.L., Lin, Y.S., Qin, J.M., Tang, W., Zhao, Z.Y., Mii, H.S., 2014. Variation in the Asian monsoon intensity and dry-wet condition since the Little Ice Age in central China revealed by an aragonite stalagmite. Clim. Past 10, 1803–1816. http://dx.doi.org/10.5194/cp-10-1803-2014.

Zhang, D.E., Li, H.-C., Ku, T.-L., Lu, L.H., 2010. On linking climate to Chinese dynastic change: spatial and temporal variations of monsoonal rain. Chin. Sci. Bull. 55, 77–83.

Zhao, M., Li, H.-C., Liu, Z.-H., Mii, H.-S., Sun, H.-S., Shen, C.-C., 2015. Changes in climate and vegetation of central Guizhou in southwest China since the last glacial reflected by stalagmite records from Yelang Cave. J Asian Earth Sci. 114, 549–561.